

Refined climatologies of future precipitation over High Mountain Asia using probabilistic ensemble learning

Kenza Tazi^{1,2}, Sun Woo P. Kim³, Marc Girona-Mata^{1,2},
Richard E. Turner¹

¹ Department of Engineering, University of Cambridge, Cambridge, United Kingdom

² British Antarctic Survey, Cambridge, United Kingdom

³ Department of Physics, King's College London, London, United Kingdom

E-mail: kt484@cam.ac.uk

Abstract. High Mountain Asia holds the largest concentration of frozen water outside the polar regions, serving as a crucial water source for more than 1.9 billion people. In the face of climate change, precipitation represents the largest source of uncertainty for hydrological modelling in this area. Future precipitation predictions remain challenging due to complex orography, lack of in situ hydrological observations, and limitations in climate model resolution and parametrisation for this region. To address the uncertainty posed by these challenges, climate models are often aggregated into multi-model ensembles. While multi-model ensembles are known to improve the predictive accuracy and analysis of future climate projections, consensus regarding how models are aggregated is lacking. In this study, we propose a probabilistic machine learning framework to combine 13 regional climate models from the Coordinated Regional Downscaling Experiment (CORDEX) over High Mountain Asia. Our approach accounts for seasonal and spatial biases within the models, enabling the prediction of more faithful precipitation distributions. The framework is validated against gridded historical precipitation data and is used to generate projections for the near future (2036–2065) and far future (2066–2095) under RCP4.5 and RCP8.5 scenarios.

Keywords: High Mountain Asia, precipitation, ensemble learning, regional climate models, probabilistic, mixture of experts, Gaussian process, CORDEX-WAS

1. Introduction

The glaciers and snowfields of High Mountain Asia (HMA), shown in Figure 1, store more frozen water than anywhere else in the world after the Arctic and Antarctic polar caps. These mountains provide fresh water for more than 1.9 billion people through Asia’s major rivers (Immerzeel et al., 2020). Despite the importance of these water resources, much remains unknown about their distribution and how they will evolve under climate change. Precipitation remains the largest source of uncertainty for modelling future water security over HMA (Nie et al., 2021; Orr et al., 2022; Wester et al., 2023). Regional climate models (RCMs) are the main tool for understanding future precipitation over HMA (Maussion et al., 2014; Norris et al., 2017, 2019; Orr et al., 2017; Norris et al., 2020; Palazzi et al., 2015). However, complex orography and the lack of in situ hydrological observations, combined with limited RCM resolution and parametrisations, make precipitation difficult to model in this region (Tazi et al., 2024, 2025; Girona-Mata et al., 2024). To overcome these challenges and understand the range of possible changes in precipitation, different RCMs with different physics and model parametrisations are run, and their outputs combined.

Such collections of climate models are known as multi-model ensembles. In general, multi-model ensembles improve the accuracy of historical predictions and provide a way to explore the uncertainties in model-based climate projections (Palmer et al., 2005; Stainforth et al., 2007; Kharin and Zwiers, 2002). However, the way in which models are combined is controversial (Tebaldi and Knutti, 2007). This includes disagreements about how to measure the aggregate accuracy (Eyring et al., 2019), deal with ensemble outliers (Sanderson and Knutti, 2012), account for the proximity of model design (Masson and Knutti, 2011; Knutti, 2010), and address an infinite number of possible ensemble members (Tél et al., 2020). As a result, the Intergovernmental Panel on Climate Change has previously opted for the unweighted average of the global climate models (GCMs) from the Climate Model Intercomparison Project (CMIP) in their previous reports, using model spread as the uncertainty for future predictions (Flato et al., 2014).[‡]

In this paper, we present a probabilistic machine learning framework with the aim of statistically downscaling and combining precipitation outputs from 13 RCMs from the Regional Downscaling Experiment (CORDEX). This method leverages the RCMs’ heterogeneous seasonal and spatial biases to generate precipitation probability distributions for any location and month. This is achieved through a two-step approach. First, we compute statistical surrogates of the RCMs. For a given climatological period, we compile the empirical precipitation distribution for each RCM, location, and month. Then, we model the empirical distributions with Gaussian processes (GPs). GPs have been used in previous research for similar settings, such as spatiotemporal aggregation of GCMs using deep kernel learning (Harris et al., 2013) or to find the latent signal of

[‡] The sixth report (AR6) discards ‘hot-models’ from CMIP6 that have been shown to be overly sensitive to emission forcing (Zelinka et al., 2020; Hausfather et al., 2022; Lee et al., 2021).

a temperature change in GCM ensembles for a single location (Amos et al., 2022).

Second, we aggregate the RCM surrogate predictions at each spatiotemporal point via a mixture of experts (MoE), where distributions of experts (i.e. RCM surrogates) are combined using weights. We parametrise the weight of each expert by their Wasserstein distance with respect to historical data (APHRODITE) and a learnt ‘statistical temperature’. Our ensemble learning method is therefore similar to Bayesian model averaging (Massoud et al., 2023; Min et al., 2007; Olson et al., 2016), where the similarity of the probability distribution with respect to historical data is used as a measure of faithfulness. However, unlike previous ensembling techniques, our method neither gives each RCM one vote (i.e. equal weighting), nor does it completely discard outliers with less accurate distributions, only down-weight them. As more experts are added, more precipitation events can be considered, and the final distribution refined.

The paper is structured as follows. The study area and data are first described in Section 2. The method is then summarised in Section 3 and validated in Section 4. Predictions for a historical reference period (1976–2005), the near future (2036–2065), and the far future (2066–2095) for RCP4.5 and RCP8.5 are analysed in Section 5. Finally, limitations and further work are discussed in Section 6.

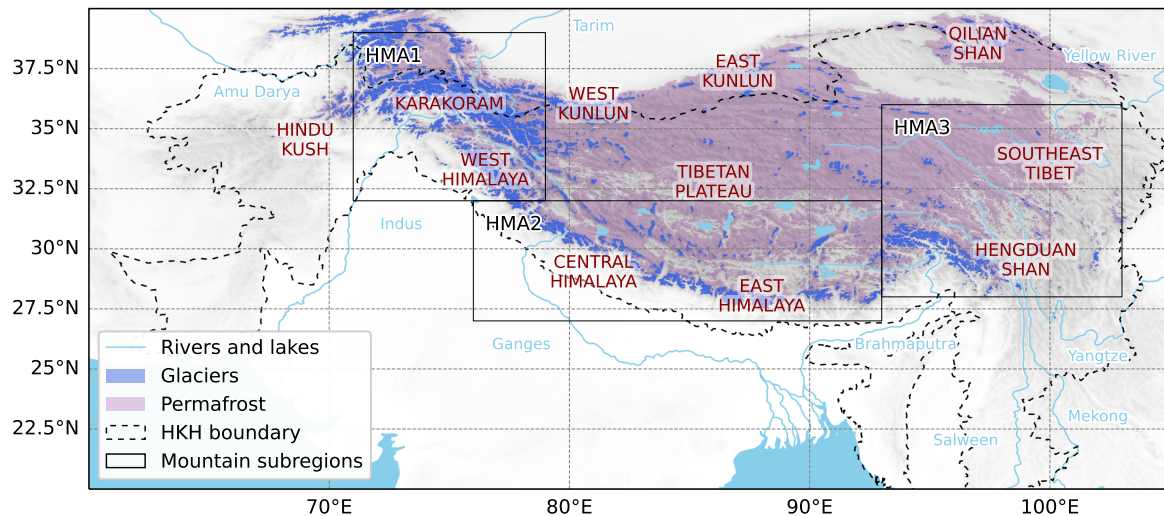


Figure 1. Map of High Mountain Asia showing major rivers and lakes (Lehner and Grill, 2013), glaciers (RGI Consortium, 2017), permafrost (Westermann et al., 2024), the HKH boundary as defined by ICIMOD (2008), and three mountain subregions used for this study: the West Himalaya and Karakoram (HMA1), the Central and East Himalaya (HMA2), the Hengduan Shan and Southeast Tibet (HMA3). The map also includes the standardised names of glacierised mountains regions (GTN-G, 2023) referenced in this paper.

2. Study area and datasets

2.0.1. Study area Following Sanjay et al. (2017), we study precipitation over HMA between 20°–40°N 60°–100°E as shown in Figure 1 and three mountain subregions: the West Himalaya and Karakoram (HMA1, 32°–39°N 71°–79°E), the Central and East Himalaya (HMA2, 27°–32°N 76°–93°E), and the Hengduan Shan and Southeast Tibet (HMA3, 27°–32°N 93°–103°E). In addition to including most glaciers for HMA, these subregions are representative of synoptic precipitation patterns driven by western disturbances for HMA1 over winter (December to March) and the Indian summer monsoon for HMA2 and the East Asian summer monsoon for HMA3 over summer (June to September). This area overlaps the Hindu Kush Himalayan (HKH) region. As defined by the International Centre for Integrated Mountain Development, the HKH extends from 16° to 39°N and 61° to 105°E and encompasses more than 4 192 000 km² of mountains over Afghanistan, Bangladesh, Bhutan, China, India, Myanmar, Nepal, and Pakistan (Bajracharya and Shrestha, 2011).

2.0.2. CORDEX-WAS CORDEX is a global initiative that aims to provide high-resolution climate data for regional and local applications. CORDEX for the West Asia domain (CORDEX-WAS, –20°–50°N 20°–115°E), also known as the South Asia domain, uses RCMs to dynamically downscale global climate simulations from the fifth CMIP (CMIP5) over most of HMA (Sanjay et al., 2017; Taylor et al., 2012). CORDEX-WAS outputs are chosen over other RCM simulations for their accessibility and rigorous experimental protocol (Giorgi and Gutowski Jr, 2015), which allow for the straightforward comparison of many models. CORDEX-WAS is made up of 13 models using three RCMs and ten driving CMIP5 GCMs, as listed in Table 1.

The CORDEX outputs are stored on a 0.44° rotated grid (approximately 50km resolution). However, for simplicity, we use interpolated outputs on a 0.5° regular grid. We analyse CORDEX-WAS monthly precipitation outputs over 20°–40°N and 60°–105°E for historical (1950–2005) and projected (2006–2100) scenarios. Historical experiments use estimates of greenhouse gas concentrations, aerosols, and land use (from observed or reconstructed data) to drive the GCMs. Future projected experiments are based on representative carbon pathways (RCPs), i.e., theoretical future emissions scenarios. In this paper, outputs for RCP4.5 and RCP8.5 are investigated. RCP4.5 represents a stabilisation pathway, where emissions peak around 2040 and then decline, while RCP8.5 represents a high-emissions pathway with minimal policy intervention. Going forward, we simplify simulation names to ‘GCM RCM’, e.g. the IITM-RegCM4 simulation driven by IPSL-CM5A-LR becomes IPSL RegCM4.

2.0.3. APHRODITE The Asian Precipitation-Highly Resolved Observational Data Integration Towards Evaluation of Water Resources (APHRODITE) dataset is a gridded precipitation dataset ranging from 1951 to 2015 with a spatial resolution of 0.25°

Table 1. CORDEX-WAS RCMs with CMIP5 driving models. Note that GFDL-ESM2M, MPI-ESM-LR, and CNRM-CM5 each drive two RCMs. †The SMHI-RCA4 CNRM-CM5 model output only extends to 2085 for RCP8.5. ‡MPI-REMO2009 MPI-ESM-LR model output only begins from 1961.

RCM	Driving CMIP5 model
IITM-RegCM4 (Giorgi et al., 2012)	CanESM2 (Chylek et al., 2011) GFDL-ESM2M (Dunne et al., 2012) CNRM-CM5 (Voldoire et al., 2013) MPI-ESM-MR (Jungclaus et al., 2013) IPSL-CM5A-LR (Dufresne et al., 2013) CSIRO-Mk3.6 (Jeffrey et al., 2013)
SMHI-RCA4 (Samuelsson et al., 2015)	EC-Earth (Hazeleger et al., 2010) MIROC5 (Watanabe et al., 2010) MPI-ESM-LR (Jungclaus et al., 2013) IPSL-CM5A-MR (Dufresne et al., 2013) GFDL-ESM2M CNRM-CM5†
MPI-REMO2009 (Teichmann et al., 2013)	MPI-ESM-LR‡

(Yatagai et al., 2012). In general, APHRODITE has one of the best spatiotemporal coverage of precipitation products over High Mountain Asia and is one of the most studied and accurate products for the region (Dimri, 2021). The dataset was created through the interpolation of precipitation gauge observations using a custom correlation distance lookup table. We use the monthly precipitation product APHRO_V1101 specifically developed for monsoon Asia. Figure 2 plots APHRODITE precipitation between 1976 and 2005.

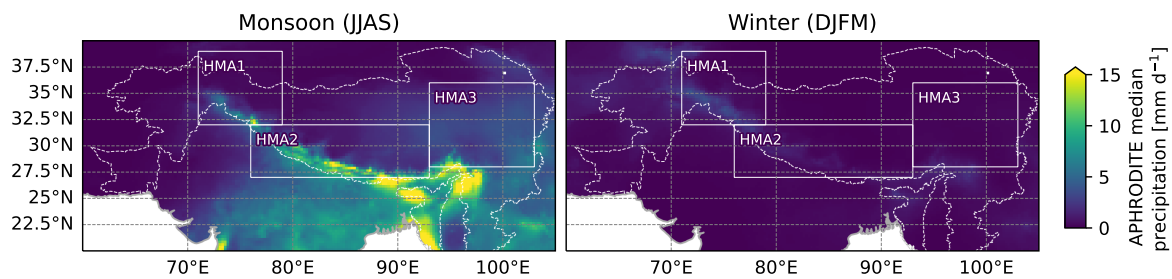


Figure 2. APHRODITE precipitation medians between 1976 and 2005 for the monsoon (left) and winter (right).

3. Method

This section details our ensemble learning method, outlined in Figure 3.

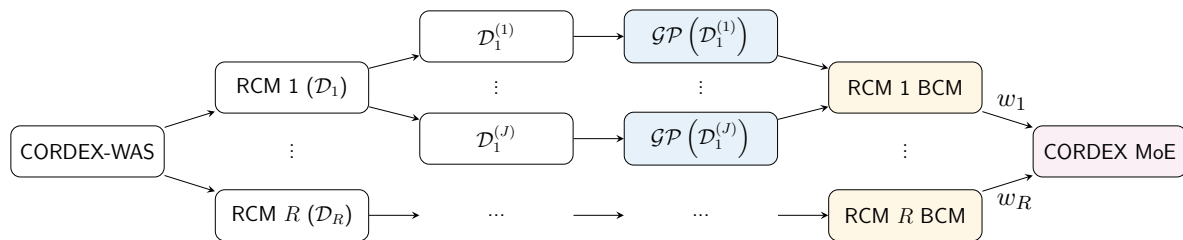


Figure 3. Ensemble learning method. For a given emission scenario and climatological period, each of the R RCMs outputs from CORDEX-WAS are split into J manageable spatiotemporal domains, $\mathcal{D}_1^{(j)}$ for the j th domain and r th RCM. A GP is fit to each domain and then combined using a BCM. The outputs of each RCM GP are then combined using a weighted mixture model or mixture-of-experts (MoE) with weights w_r .

3.1. RCM surrogate models

3.1.1. Gaussian processes To create the surrogate models for each RCM, we consider a regression problem with a dataset of N paired inputs $\mathbf{X} := \{\mathbf{x}_i\}_{i=1}^N$ and noisy observations $\mathbf{Y} := \{y_i\}_{i=1}^N$, where i denotes the i th data pair. Each input \mathbf{x}_i is a three-dimensional vector of (month, latitude, longitude). Each observation y_i is a scalar, corresponding to a prediction of precipitation by an RCM.

The problem is modelled as $y_i = f(\mathbf{x}_i) + \epsilon_i$, where we assume that the noise $\epsilon_i \sim \mathcal{N}(\mathbf{0}, \sigma_n^2)$ is independently and identically distributed. The function f can be represented with a Gaussian process (GP) (Rasmussen and Williams, 2006). GPs are powerful non-parametric Bayesian models. A GP is defined as a distribution over functions such that every finite set of inputs and outputs is jointly Gaussian distributed. GPs are fully defined by a mean function $\mu(\cdot)$ and a kernel function $k(\cdot, \cdot)$, which depend on hyperparameters θ_μ and θ_k , jointly referred to as θ .

If we assume f to be a GP, i.e. $f \sim \mathcal{GP}(\mu(\cdot), k(\cdot, \cdot))$, it follows that $f(\mathbf{X}) \sim \mathcal{N}(\boldsymbol{\mu}_\mathbf{X}, \mathbf{K}_\mathbf{X} + \sigma_n^2 \mathbf{I})$ where $(\boldsymbol{\mu}_\mathbf{X})_i := \mu(\mathbf{x}_i)$ is a N -dimensional vector and $(\mathbf{K}_\mathbf{X})_{ij} = k(\mathbf{x}_i, \mathbf{x}_j)$ is an $N \times N$ covariance matrix. We infer a posterior GP conditioned on the dataset $\mathcal{D} = (\mathbf{X}, \mathbf{Y})$. The mean and variance of the posterior predictive distribution of f , evaluated at a test point \mathbf{x}_* , are given by

$$\mathbb{E}_{f|\mathcal{D}}[f(\mathbf{x}_*)] = \mu(\mathbf{x}_*) + \mathbf{K}_*^T (\mathbf{K}_\mathbf{X} + \sigma_n^2 \mathbf{I})^{-1} (\mathbf{Y} - \boldsymbol{\mu}_\mathbf{X}), \quad (1)$$

$$\text{Var}_{f|\mathcal{D}}[f(\mathbf{x}_*)] = k(\mathbf{x}_*, \mathbf{x}_*) - \mathbf{K}_*^T (\mathbf{K}_\mathbf{X} + \sigma_n^2 \mathbf{I})^{-1} \mathbf{K}_*, \quad (2)$$

where $\mathbf{K}_* = k(\mathbf{X}, \mathbf{x}_*)$ is an N -dimensional vector. Kernel hyperparameters are learnt by maximising the log-marginal likelihood,

$$\hat{\theta} = \underset{\theta}{\text{argmax}} [\log p(\mathbf{Y}|\mathbf{X}, \theta)] = \underset{\theta}{\text{argmax}} [\log \mathcal{N}(\mathbf{Y}|\boldsymbol{\mu}_\mathbf{X}(\theta_\mu), \mathbf{K}_\mathbf{X}(\theta_k) + \sigma_n^2 \mathbf{I})]. \quad (3)$$

Once a distribution is modelled as a GP, it can be evaluated at any inputs. Therefore, GPs can be used to interpolate empirical distributions. To compare the RCM surrogates with the APHRODITE dataset introduced in Section 2.0.3, we evaluate the surrogate GPs at the APHRODITE grid points.

3.1.2. Warped GP In its original formulation, the posterior distribution of the GP is normal. However, monthly precipitation y is generally log-normally distributed (Tazi et al., 2024). Warped GPs handle non-normality in the data by transforming the target variables and GP outputs via a warping function (Snelson et al., 2003). For this problem, we use a Box-Cox function $g_\lambda(\cdot)$ as the warping function. The warped outputs \tilde{y} are then given by

$$\tilde{y} = g_\lambda(y) = \begin{cases} \frac{y^\lambda - 1}{\lambda} & \text{for } \lambda \neq 0, \\ \log y & \text{for } \lambda = 0, \end{cases} \quad (4)$$

where precipitation $y > 0$ is assumed to be positive and λ is the scaling factor. The scaling factor is optimised to make the distribution of $g_\lambda(y)$ as Gaussian as possible by maximising the log-likelihood of the model parameters arising from placing a Gaussian distribution over the transformed observations (Box and Cox, 1964). In this study, we use a different optimised scaling factor λ_r for each RCM r . Henceforth, we will use $f(\cdot)$ to denote the function that models the *warped* output \tilde{y} . We will denote the unwarped function, which may have heavy tails in its distribution, as $f_\lambda(\cdot) := g_\lambda^{-1}(f(\cdot))$. Details on the distribution of the unwarped precipitation can be found in Appendix B.

3.1.3. Chained GP For this application, the variance of precipitation y should be considered as intrinsic climatological variance rather than noise. The GP output should therefore be heterogeneous in its variance, i.e. heteroskedastic. To address these requirements, we use chained GPs (Saul et al., 2016) to model the variance and mean as latent functions such that

$$p(\tilde{y}_i | f_1, f_2, \mathbf{x}_i) = \mathcal{N}\left(\tilde{y}_i \mid f_1(\mathbf{x}_i), \alpha(f_2(\mathbf{x}_i))\right), \quad (5)$$

where $f_1 \sim \mathcal{GP}(0, k_1(\cdot, \cdot))$, $f_2 \sim \mathcal{GP}(0, k_1(\cdot, \cdot))$ and α is a function used to map the outputs of f_2 to positive values. This mapping is required as the output of α represents the variance of a Gaussian distribution. Here, we apply an exponential function $\alpha(f_2(\mathbf{x}_i)) = e^{f_2(\mathbf{x}_i)}$, but other functions, such as softplus, could be used. For our work, we use a shortcut to calculate the variance at each point without using further approximations, such as inducing points (Titsias, 2009), by exploiting the gridded nature of our data.

3.1.4. Bayesian committee machine Due to GP’s poor scalability to large datasets, we use robust Bayesian committee machines (BCMs) as a way of combining multiple GPs and speeding up inference (Tresp, 2000; Deisenroth and Ng, 2015; Cohen et al., 2020). To do this, the training dataset is partitioned into J subsets of size M (so

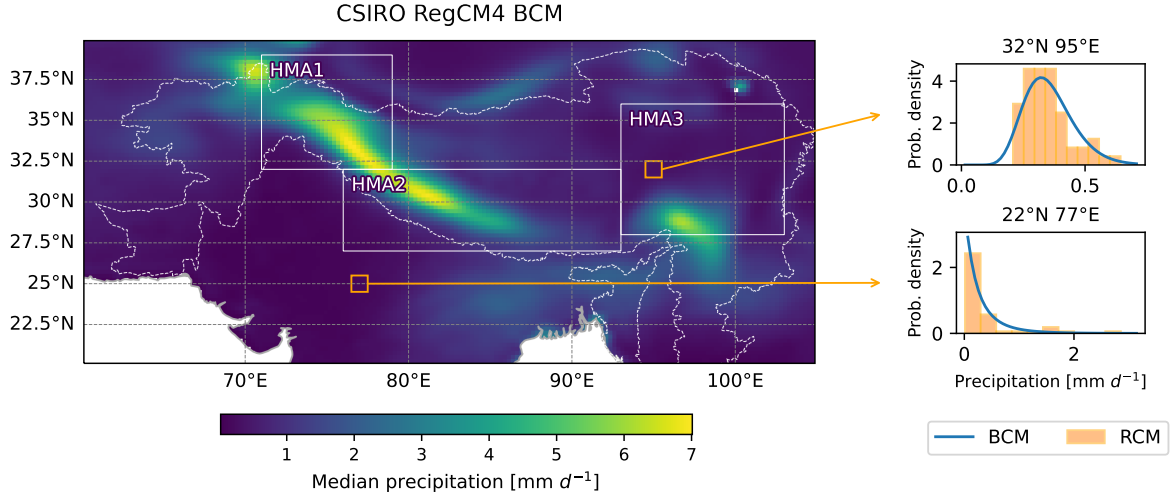


Figure 4. CSIRO RegCM4 BCM distributions between 1951 and 2005 for the month of February. The figure shows the median of the surrogate distributions over HMA (left) The surrogate distributions (blue line) are compared with the empirical histograms (orange bar) for two example locations (top and bottom right). The full surrogate distributions are faithful to the original RCM distributions, which differ significantly depending on time and location.

$N = JM$) where $M \ll N$. We define these subsets or domains as $\mathcal{D}^{(j)} = (\mathbf{X}^{(j)}, \mathbf{Y}^{(j)})$ for $j = 1, \dots, J$. GPs are then used to model each domain. The robust BCM GPs share kernel hyperparameters, stopping individual experts from overfitting their local subset of data. Assuming conditional independence between domains $\mathcal{D}^{(j)}$ and by repeated application of Bayes' theorem, the following predictive distribution is obtained by combining the separate GP models:

$$p(f(\mathbf{x}_*)|\mathcal{D}) = \frac{\prod_{j=1}^J p_j^{\beta_j(\mathbf{x}_*)}(f(\mathbf{x}_*)|\mathcal{D}^{(j)})}{p^{-1+\sum_j \beta_j(\mathbf{x}_*)}(f(\mathbf{x}_*))}, \quad (6)$$

where $p(f(\mathbf{x}_*))$ is the prior distribution of the GP evaluated at test point \mathbf{x}_* and β_j controls the contribution of expert j (see Appendix A). The robust BCM's predictive mean and precision (inverse of the variance) are given by

$$\mu_*^{\text{rbcm}} := \mathbb{E}_{f|\mathcal{D}^{(1)}\dots\mathcal{D}^{(j)}} [f(\mathbf{x}_*)] = (\sigma_*^{\text{rbcm}})^2 \sum_{j=1}^J \beta_j(\mathbf{x}_*) (\sigma_*^j)^{-2} \mu_*^j, \quad (7)$$

$$(\sigma_*^{\text{rbcm}})^{-2} := \text{Var}_{f|\mathcal{D}^{(1)}\dots\mathcal{D}^{(j)}} [f(\mathbf{x}_*)]^{-1} = (1 - M)(\sigma_*^{\text{prior}})^{-2} + \sum_{j=1}^J \beta_j(\mathbf{x}_*) (\sigma_*^j)^{-2}, \quad (8)$$

respectively, where μ_*^j and $(\sigma_*^j)^{-2}$ are the mean and precision of the predictive posterior given domain $\mathcal{D}^{(j)}$, and $(\sigma_*^{\text{prior}})^{-2}$ is the prior precision of $p(f_*)$. This setup conserves the properties of an exact GP while improving scalability, moving from $\mathcal{O}(N^3)$ for training and $\mathcal{O}(N^2)$ for prediction to $\mathcal{O}(JM^3)$ and $\mathcal{O}(JM^2)$ respectively (Deisenroth

and Ng, 2015). For our work, the domains are divided temporally, such that each domain contains precipitation for a particular month over the whole spatial area. In Figure 4, we illustrate the typical surrogate output with CSIRO RegCM4 for February. The surrogate distributions closely match the empirical RCM histograms, which can significantly differ depending on time and location.

3.2. Surrogate aggregation

3.2.1. Mixture of experts The outputs of the RCM surrogates are aggregated via the weighted sum of their posterior probability distributions. We refer to this weighted mixture model as a mixture of experts (MoE). The resulting distribution for a given test point \mathbf{x}_* is

$$p_{\text{MoE}}(f_{\lambda}(\mathbf{x}_*)|\mathbf{w}, \mathcal{D}) = \sum_{r=1}^R w_r p_r(f_{\lambda_r}(\mathbf{x}_*)|\mathcal{D}_r). \quad (9)$$

Here, \mathcal{D} is the dataset for all RCMs, and \mathcal{D}_r is the dataset for the r^{th} RCM for $r = 1, \dots, R$. $p_r(f_{\lambda_r}(\mathbf{x}_*)|\mathcal{D}_r)$ is the *unwarped* r^{th} RCM surrogate distribution conditioned on \mathcal{D}_r . It is *not* Gaussian and depends on the warping parameter λ_r . $w_r = w_r(\mathbf{x}_*)$ is the weight of the r^{th} RCM at \mathbf{x}_* . It is constrained to be $\sum_{r=1}^R w_r = 1$ and $w_r > 0$.

3.2.2. Weights We would like to choose weights \mathbf{w} such that the MoE accurately predicts future and past precipitation distributions. Without prior knowledge, the simplest weighting would be $w_r = 1/R$, i.e. an equally-weighted (EW) mixture of the RCM surrogates, not assigning more importance to any particular RCM. Instead, we inform the weights through a reference dataset (APHRODITE; see Section 2.0.3), having previously downscaled RCM predictions onto the same grid using the surrogate models, as shown in Section 3.1.1 and Figure 4. A naive approach would be to directly learn the weights that maximise the likelihood of the parameters (APHRODITE). However, there are two potential pitfalls to this method. First, the number of effective parameters is $R - 1$ ($=12$), compared to the number of datapoints at each location and time (~ 30), resulted in overfitting the R model weights (not shown). Second, direct maximum likelihood optimisation could upweigh RCM surrogates that, individually predict precipitation poorly, but when summed together best approximate APHRODITE. We want to ensure that RCM surrogates that contribute significantly to the aggregate are independently close fits to APHRODITE.

Thus, we inform the weights using a measure of distance between the distribution of each RCM surrogate and that of APHRODITE. We choose the Wasserstein distance (Panaretos and Zemel, 2019), which originates from optimal transport theory and represents the minimum cost of moving the probability density of one distribution into the shape of another. For two empirical distributions P and Q , the Wasserstein distance

W is given by:

$$W(P, Q) = \left(\frac{1}{N} \sum_{i=1}^N \|X_i - Y_i\|^p \right)^{1/p}, \quad (10)$$

where X_i and Y_i are the samples of P and Q , respectively, and p is the moment of the distribution we are interested in. Here, we use the first moment $p = 1$, which represents the shift of the distribution mean. We calculate the Wasserstein distances with respect to a reference historical period for each APHRODITE grid point and month. Previous research has shown that evaluating the shapes of the distribution rather than the differences in the absolute precipitation outputs better distinguishes how well the models represent precipitation (Martinez-Villalobos and Neelin, 2021). We therefore scale the 95th percentile of the BCM outputs to match that of APHRODITE.

We then introduce the statistical temperature T , which interpolates between choosing the most accurate RCM ($T = 0$) and equally weighting the RCMs ($T \rightarrow \infty$). Using this concept, the weights are parametrised as

$$w_r = \frac{e^{-h(W_r)/T}}{\sum_{r'} e^{-h(W_{r'})/T}}, \quad (11)$$

where $h(\cdot)$ is some monotonically increasing function. The statistical temperature T is then optimised to maximise the likelihood on the APHRODITE dataset. We chose $h(\cdot) = \ln(\cdot)$, which reduces the variation between the Wasserstein distances. This choice meets our criteria for the weights to vary smoothly in space and to not choose a single RCM. To further stabilise optimisation, we maximised the likelihood around a 5×5 grid surrounding each location. The RCM surrogates with the smallest Wasserstein distances and the maximum MoE weights over HMA are shown in Appendix C.

4. MoE validation

To evaluate the performance of the MoE approach relative to the EW, the historical experiment is divided into two sets: a training period (1951–1980) and a validation period (1981–2005). We use the continuous rank probability score (CRPS, ?), which measures the distance between the predicted (MoE or EW) and observed (APHRODITE) cumulative distribution functions (CDF) F . The CRPS is defined as the integral of the squared difference between the predicted CDF $F(y)$ and the observed CDF $F_{\text{obs}}(y)$ over the range of possible values y :

$$\text{CRPS} = \int_{-\infty}^{\infty} (F(y) - F_{\text{obs}}(y))^2 dy. \quad (12)$$

Smaller scores therefore imply more skill.

The spatiotemporal distribution of the differences between the MoE and EW CRPS are presented in Figure 5. The MoE CRPS values are on average smaller than the EW

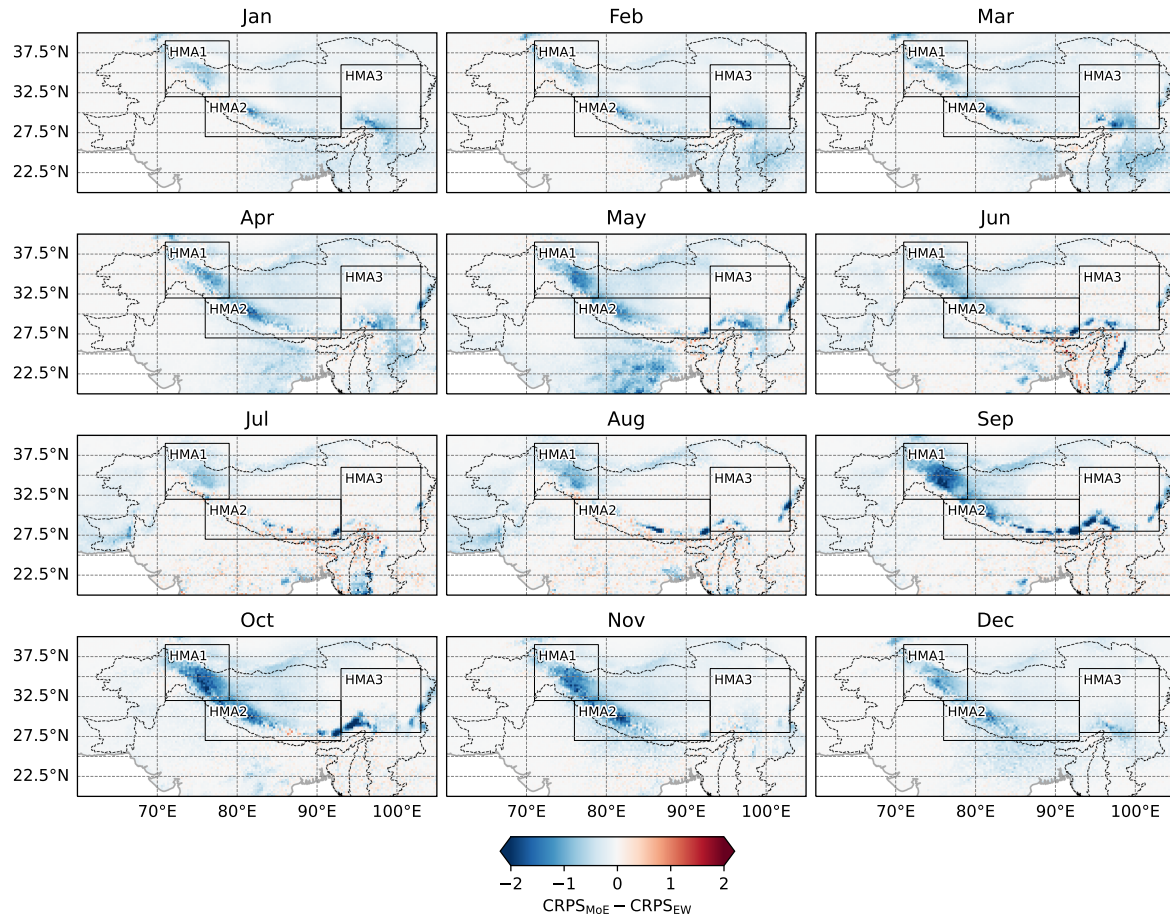


Figure 5. MoE and EW CRPS differences over the held-out validation period (1981–2005). Negative values (blue) imply MoE matches APHRODITE more closely while positive values (red) represent times and location where the EW performs better. The MoE outperforms the EW for each month, in particular over the Karakoram and Himalayan arc.

CRPS values, showing that the MoE approach yields significant improvements compared to EW. The greatest improvements are over the Karakoram mountains and Himalayas, with an annual average difference of -0.34 for the West Himalaya and Karakoram (HMA1), -0.24 for the Central and East Himalaya (HMA2), and -0.14 for the Hengduan Shan and Southeast Tibet (HMA3); while EW is sometimes more advantageous over the south Himalaya during the summer months. Areas where no significant change in score is observed tend to correspond to locations where the MoE learns a close-to-equal weighting (see Figure C2). The MoE also improves over taking any individual expert, i.e. the RCM surrogates, as shown in Figures D1 and D2.

5. Refined climatologies

To generate refined historical and future climatologies, we optimise the weights over the entire historical period (1951–2005), thus maximising data availability. We then

use these weights to generate MoE ensemble predictions for the same climate scenarios and time periods as Sanjay et al. (2017): i) historical (1976–2005), ii) RCP4.5 near (2036–2065) and future (2066–2095), and iii) RCP8.5 near and far future. In the following analysis, we focus on historical and far-future periods to generate projected precipitation trends relative to a historical baseline. The near-future projections show trends comparable to the far future, but with less pronounced changes, and are included in Appendix E.

5.1. Historical predictions

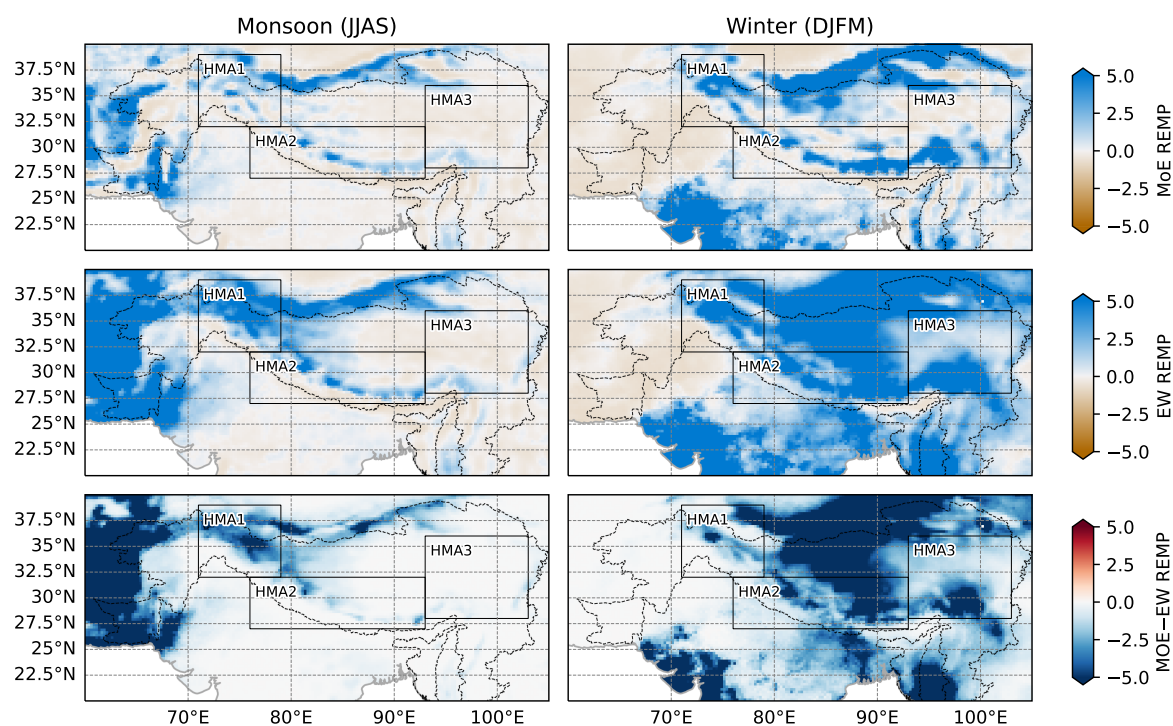


Figure 6. Historical MoE and EW relative error for median precipitation (REMP) with respect to APHRODITE over HMA. The MoE REMP (top), the EW REMP (middle), and the REMP difference between MoE and EW (bottom) are plotted for the historical reference period (1976–2005) for the monsoon (left) and winter (right). The MoE makes large improvements over the EW, in particular, over locations where precipitation is overestimated by the EW.

Figure 6 plots the relative error for median precipitation (REMP) for the MoE and EW with respect to APHRODITE for the historical period. For the monsoon season, the MoE and EW both under- and overestimate precipitation for the Himalaya and Karakoram (HMA1 and HMA2). More specifically, the models predict a wet bias for the Karakoram, inner Himalayas, and western Tibetan Plateau and a dry bias for the outer Himalayas. Precipitation over the eastern Tibetan Plateau, Hengduan Shan, and Southeast Tibet (HMA3) is generally underestimated by both models. For winter, the MoE under- and overestimates precipitation across the three studied subregions with

greater wet biases, including the Tibetan Plateau and Hengduan Shan. On the other hand, the EW scheme largely overestimates precipitation across all three areas during winter.

The third row of Figure 6 shows that the MoE makes large improvements over EW, particularly over locations where the EW overestimates precipitation. This corresponds to a difference in relative error of 2.02 for the West Himalaya and Karakoram (HMA1), 0.32 for the Central and East Himalaya (HMA2), and 0.08 for the Hengduan Shan and Southeast Tibet (HMA3) over the summer. During winter, larger improvements are obtained with relative error differences of 1.58, 3.02, and 2.33 for the West Himalaya and Karakoram (HMA1), the Central and East Himalaya (HMA2), and the Hengduan Shan and Southeast Tibet (HMA3), respectively. In summary, the MoE predicts smaller median precipitation values compared to the EW, more in line with APHRODITE. However, MoE predictions are still subject to large errors, and bias correction would still be needed before use.

5.2. Future projections

Figure 7 shows far-future MoE projections with respect to the historical period. For RCP4.5 and RCP8.5, the monsoon season is projected to see an increase in median precipitation over most of HMA, with the exception of the north Hindu Kush mountains. The greatest changes occur over Kunlun mountains and Southeast Tibet. More specifically, the MoE predicts an average increase of 15% for the West Himalaya and Karakoram (HMA1), 23% for the Central and East Himalaya (HMA2), and 27% for the Hengduan Shan and Southeast Tibet (HMA3) for RCP8.5. Compared to RCP4.5, RCP8.5 presents a more pronounced wetting trend over the study area.

For winter, the MoE projects an increase in median precipitation over the north and northeast HKH, with the largest changes occurring over the Quilian Shan and East Kunlun mountains. The Hindu Kush mountains and the outer Himalayas show an overall decrease in precipitation for this season. These trends lead to mixed predictions for the West Himalaya and Karakoram (HMA1) and the Central and East Himalaya (HMA2), with average relative changes of 15% and -7% for RCP8.5, respectively. Winter precipitation over the Hengduan Shan and Southeast Tibet (HMA3) is expected to increase with an average relative change of 27%. Compared to RCP4.5, RCP8.5 generally presents more pronounced wetting and drying trends during winter.

Finally, the relative changes in precipitation from the MoE can be compared with those from the EW. Figure 8 plots the difference between the MoE and EW relative changes for the far-future RCP4.5 and RCP8.5 scenarios. The plot shows that for large areas, including the Tibetan Plateau over summer and the Hindu Kush, the relative precipitation changes predicted by the MoE and the EW stay within $\pm 10\%$ across different percentiles. However, many locations also present significant changes.

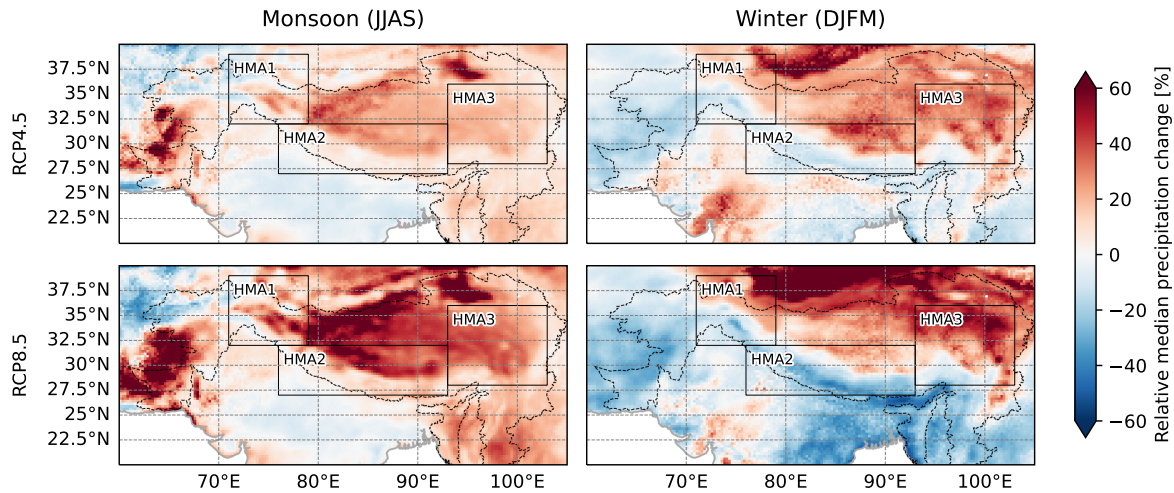


Figure 7. Relative changes between far-future (2066–2095) and historical (1976–2005) MoE precipitation. The plot shows the median changes for RCP4.5 (top) and RCP8.5 (bottom) over the monsoon (left) and winter (right) for the far-future across HMA. The MoE predicts large departures from the precipitation predicted for the historical reference period.

During the monsoon, positive differences in predicted precipitation changes (i.e., MoE increase relative to EW) are observed over the West Himalaya, Karakoram and Kunlun mountains with median and 95th percentile differences reaching maximum values of 54% and 32% for HMA1. This suggests that the probability of events associated with very high precipitation rates, such as floods and landslides, could be higher compared to previous estimates. During winter, the MoE predicts a greater decrease in projected precipitation over the inner Himalayas and Karakoram, with median differences achieving minimum values of -31% for HMA1 and -27% for HMA2. This could signify a decrease in the contribution of winter precipitation to solid water resources. At the same time, large positive differences are observed over the Tibetan Plateau and Southeast Tibet, with maximum differences in median values of 51% for HMA2 and 62% for HMA3.

6. Discussion

This paper has explored a probabilistic ensemble learning approach to aggregating RCMs using a MoE approach, with the aim of improving future precipitation projections over using the EW. Unlike other ensembling techniques, our method does not narrow the non-discountable envelope of climate change, but refines it. With GPs as its foundational building blocks, this method should work equally well with RCMs on different grids and can be straightforwardly applied to any kind of model ensemble. However, this study does present several limitations.

First, we assume that precipitation from the driving GCMs is sufficiently well-modelled

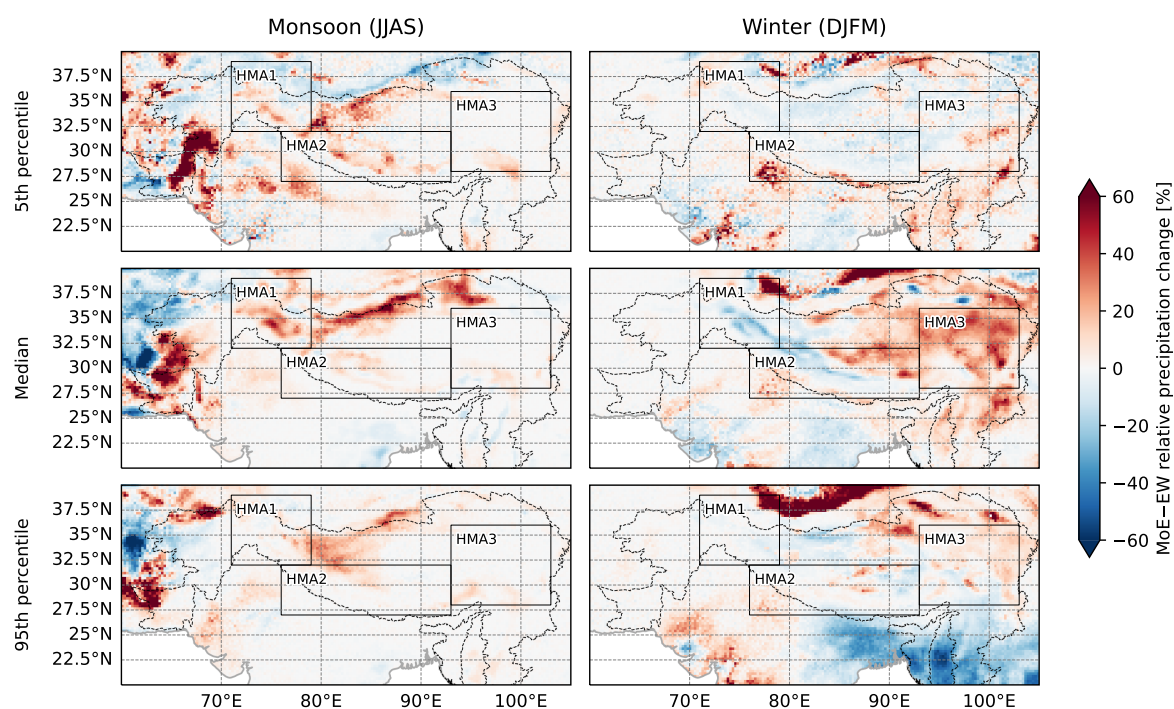


Figure 8. MoE and EW prediction differences for the far future (2066–2095) under RCP8.5 across HMA. The plot shows the differences between the predicted relative changes for the 5th percentile (bottom), median (middle), and 95th (top) during the monsoon (left) and winter (right). Although for many locations the MoE and EW projections are similar, there are significant difference in predictions during both the monsoon and winter over key mountain ranges.

to be dynamically downscaled. In reality, CMIP5 GCMs present large differences in their precipitation predictions over HMA (Panday et al., 2015; Palazzi et al., 2015). Moreover, recent studies incorporating more realistic aerosol scenarios further amplify future precipitation uncertainty (Jiang et al., 2023; Wilcox et al., 2020). The poor representation of precipitation in GCMs can be observed in this study through the optimal weights chosen by the MoE: when no model in the ensemble performs particularly well, the MoE chooses weights close to the EW. This is the case for the Hindu Kush during winter and for the Tibetan Plateau during summer (cf. Figure 6 and Figure C2). This behaviour, in turn, implies poor representation of two main precipitation drivers for HMA: the East Asian summer monsoon and western disturbances. Further work could use this framework to explain performance differences across RCMs by analysing other output variables, such as pressure or humidity fields.

Second, the methods used to create the RCM surrogates have several limitations. By applying GPs, we assume that the RCM outputs are unimodal. In reality, this is not always the case, and we could be missing out on inter-annual variability. This problem is further compounded through the monthly aggregation of the RCM data. Using a probabilistic surrogate for the RCM means that future precipitation scenarios

can be sampled thanks to the correlations learnt between different locations and times. However, the degree to which the samples are consistent in time is uncertain. By aggregating data over time, the RCM surrogate, and by extension the MoE, could plausibly sample two high precipitation values for neighbouring locations or months, although the joint event is statistically unlikely. Reintroducing some of the information from the RCM time series would be needed to ensure further consistency.

Third, the weighting function used to aggregate the RCMs, although well motivated, has an arbitrary form. There is significant room to refine the approach through more case studies. Finally, monthly precipitation is not the only variable linked to water security over HMA. To get a more holistic view of future changes, and thus the risk of extreme events such as floods and droughts, the experiments in this paper could be repeated with variables such as temperature or the number of cumulative dry and wet days. Extreme value analysis could also be applied to calculate updated rates of return for single or compounding hydrological extremes.

7. Conclusion

This paper investigated a mixture of experts (MoE) approach to aggregate an ensemble of RCMs. This ensemble learning method is generalisable to other climate variables and model ensembles and could be applied to model aggregation problems in other fields. The MoE was applied to the CORDEX-WAS ensemble over HMA and was found to be more accurate than the equally-weighted average (EW) or any single ensemble member for a held-out validation period. Compared to the EW, the MoE projects a significantly wetter summer but a drier winter over the western Himalayas and Karakoram and a significantly wetter winter over the Tibetan Plateau, Hengduan Shan, and South East Tibet for both the near and far future under RCP4.5 and RCP8.5.

Software and data accessibility

The code and data for this paper are available on GitHub (<https://github.com/kenzaxtazi/bcm4rcm>). The CORDEX-WAS data are available through the Earth System Federation Grid nodes <https://esgf-metagrid.cloud.dkrz.de> and the APHRODITE data through the APHRODITE's Water Resources website <http://aphrodite.st.hirosaki-u.ac.jp/download/>.

Acknowledgements

The authors thank Andrew Orr and Scott J. Hosking for their thoughtful feedback on the manuscript. This work was supported by the Engineering and Physical Sciences Research Council through the AI for Environmental Risk (AI4ER) CDT [grant number: EP/S022961/1] for KT and MGM, and the DTP International Studentship [grant number EP/W524475/1] for SWPK.

References

- M. Amos, T. Pinder, and P. Young. Identifying latent climate signals using sparse hierarchical Gaussian processes. In *NeurIPS 2022 Workshop on Tackling Climate Change with Machine Learning*, online, 9 December 2022. URL <https://www.climatechange.ai/papers/neurips2022/15>. Accessed 18 November 2024.
- S. R. Bajracharya and B. R. Shrestha. The status of glaciers in the Hindu Kush-Himalayan region. International Centre for Integrated Mountain Development (ICIMOD), 2011. URL <https://doi.org/10.53055/ICIMOD.551>.
- G. E. Box and D. R. Cox. An analysis of transformations. *Journal of the Royal Statistical Society: Series B (Methodological)*, 26(2):211–243, 1964. URL <https://doi.org/10.1111/j.2517-6161.1964.tb00553.x>.
- P. Chylek, J. Li, M. Dubey, M. Wang, and G. Lesins. Observed and model simulated 20th century Arctic temperature variability: Canadian earth system model CanESM2. *Atmospheric Chemistry and Physics Discussions*, 11(8):22893–22907, 2011. URL <https://doi.org/10.5194/acpd-11-22893-2011>.
- S. Cohen, R. Mbuva, T. Marwala, and M. Deisenroth. Healing products of Gaussian process experts. In *Proceedings of the 37th International Conference on Machine Learning*, volume 119 of *Proceedings of Machine Learning Research*, pages 2068–2077, online, 07 2020. PMLR. URL <https://doi.org/10.48550/arXiv.2102.07106>.
- M. Deisenroth and J. W. Ng. Distributed Gaussian processes. In *Proceedings of the 32nd International Conference on Machine Learning*, volume 37 of *Proceedings of Machine Learning Research*, pages 1481–1490, Lille, France, 07–09 Jul 2015. PMLR. URL <https://proceedings.mlr.press/v37/deisenroth15.html>. Accessed 24 January 2025.
- A. Dimri. Bias correction demonstration in two of the Indian Himalayan river basins. *Journal of Water and Climate Change*, 12(4):1297–1309, 2021. URL <https://doi.org/10.2166/wcc.2020.119>.
- J.-L. Dufresne, M.-A. Foujols, S. Denvil, A. Caubel, O. Marti, O. Aumont, Y. Balkanski, S. Bekki, H. Bellenger, R. Benshila, S. Bony, L. Bopp, P. Braconnot, P. Brockmann, P. Cadule, F. Cheruy, F. Codron, A. Cozic, D. Cugnet, N. de Noblet, J.-P. Duvel, C. Ethé, L. Fairhead, T. Fichefet, S. Flavoni, P. Friedlingstein, J.-Y. Grandpeix, L. Guez, E. Guilyardi, D. Hauglustaine, F. Hourdin, A. Idelkadi, J. Ghattas, S. Joussaume, M. Kageyama, G. Krinner, S. Labetoulle, A. Lahellec, M.-P. Lefebvre, F. Lefevre, C. Levy, Z. X. Li, J. Lloyd, F. Lott, G. Madec, M. Mancip, M. Marchand, S. Masson, Y. Meurdesoif, J. Mignot, I. Musat, S. Parouty, J. Polcher, C. Rio, M. Schulz, D. Swingedouw, S. Szopa, C. Talandier, P. Terray, and N. V. . N. Vuichard. Climate change projections using the IPSL-CM5 Earth System Model:

- from CMIP3 to CMIP5. *Climate dynamics*, 40:2123–2165, 2013. URL <https://doi.org/10.1007/s00382-012-1636-1>.
- J. P. Dunne, J. G. John, A. J. Adcroft, S. M. Griffies, R. W. Hallberg, E. Shevliakova, R. J. Stouffer, W. Cooke, K. A. Dunne, M. J. Harrison, J. P. Krasting, S. L. Malyshev, P. C. D. Milly, P. J. Phillipps, L. T. Sentman, B. L. Samuels, M. J. Spelman, M. Winton, A. T. Wittenberg, and N. Zadeh. GFDL’s ESM2 global coupled climate–carbon earth system models. part I: Physical formulation and baseline simulation characteristics. *Journal of climate*, 25(19):6646–6665, 2012. URL <https://doi.org/10.1175/JCLI-D-11-00560.1>.
- V. Eyring, P. M. Cox, G. M. Flato, P. J. Gleckler, G. Abramowitz, P. Caldwell, W. D. Collins, B. K. Gier, A. D. Hall, F. M. Hoffman, G. C. Hurtt, A. Jahn, C. D. Jones, S. A. Klein, J. P. Krasting, L. Kwiatkowski, R. Lorenz, E. Maloney, G. A. Meehl, A. G. Pendergrass, R. Pincus, A. C. Ruane, J. L. Russell, B. M. Sanderson, B. D. Santer, S. C. Sherwood, I. R. Simpson, R. J. Stouffer, and M. S. Williamson. Taking climate model evaluation to the next level. *Nature Climate Change*, 9(2):102–110, 2019. URL <https://doi.org/10.1038/s41558-018-0355-y>.
- G. Flato, J. Marotzke, B. Abiodun, P. Braconnot, S. C. Chou, W. Collins, P. Cox, F. Driouech, S. Emori, V. Eyring, C. Forest, P. Gleckler, E. Guilyardi, C. Jakob, V. Kattsov, C. Reason, and M. Rummukainen. Evaluation of climate models. In *Climate change 2013: the physical science basis. Contribution of Working Group I to the Fifth Assessment Report of the Intergovernmental Panel on Climate Change*, pages 741–866. Cambridge University Press, 2014. URL <https://doi.org/10.1017/CB09781107415324.020>.
- F. Giorgi and W. J. Gutowski Jr. Regional dynamical downscaling and the CORDEX initiative. *Annual review of environment and resources*, 40:467–490, 2015. URL <https://doi.org/10.1146/annurev-environ-102014-021217>.
- F. Giorgi, E. Coppola, F. Solmon, L. Mariotti, M. Sylla, X. Bi, N. Elguindi, G. Diro, V. Nair, G. Giuliani, U. U. Turuncoglu, S. Cozzini, I. Güttler, T. A. O’Brien, A. B. Tawfik, A. Shalaby, A. S. Zakey, A. L. Steiner, F. Stordal, L. C. Sloan, and C. Brankovic. RegCM4: model description and preliminary tests over multiple CORDEX domains. *Climate Research*, 52:7–29, 2012. URL <https://doi.org/10.3354/cr01018>.
- M. Girona-Mata, A. Orr, M. Widmann, D. Bannister, G. H. Dars, S. Hosking, J. Norris, D. Ocio, T. Phillips, J. Steiner, and T. Richard E. Probabilistic precipitation downscaling for ungauged mountain sites: a pilot study for the Hindu Kush Karakoram Himalaya. *EGUsphere*, 2024:1–33, 2024. URL <https://doi.org/10.5194/egusphere-2024-2805>.

- GTN-G. GTN-G glacier regions [Data set]. Global Terrestrial Network for Glaciers, 2023. URL <https://doi.org/10.5904/gtng-glacreg-2023-07>.
- G. R. Harris, D. M. Sexton, B. B. Booth, M. Collins, and J. M. Murphy. Probabilistic projections of transient climate change. *Climate dynamics*, 40:2937–2972, 2013. URL <https://doi.org/10.1007/s00382-012-1647-y>.
- Z. Hausfather, K. Marvel, G. A. Schmidt, J. W. Nielsen-Gammon, and M. Zelinka. Climate simulations: Recognize the ‘hot model’ problem. *Nature*, 605(7908):26–29, 2022. URL <https://doi.org/10.1038/d41586-022-01192-2>.
- W. Hazeleger, C. Severijns, T. Semmler, S. Ştefănescu, S. Yang, X. Wang, K. Wyser, E. Dutra, J. M. Baldasano, R. Bintanja, P. Bougeault, R. Caballero, A. M. L. Ekman, J. H. Christensen, B. van den Hurk, P. Jimenez, C. Jones, P. Kållberg, T. Koenigk, R. McGrath, P. Miranda, T. van Noije, T. Palmer, J. A. Parodi, T. Schmith, F. Selten, T. Storelmo, A. Sterl, H. Tapamo, M. Vancoppenolle, P. Viterbo, and U. Willén. EC-Earth: a seamless earth-system prediction approach in action. *Bulletin of the American Meteorological Society*, 91(10):1357–1364, 2010. URL <https://doi.org/10.1175/2010BAMS2877.1>.
- ICIMOD. Outline boundary of Hindu Kush Himalayan (HKH) region [data set]. International Centre for Integrated Mountain Development (ICIMOD), 2008. URL <https://doi.org/10.26066/RDS.3924>.
- W. W. Immerzeel, A. F. Lutz, M. Andrade, A. Bahl, H. Biemans, T. Bolch, S. Hyde, S. P. Brumby, B. J. Davies, A. C. Elmore, A. Emmer, M. Feng, A. Fernández, U. K. Haritashya, J. S. Kargel, M. N. Koppes, P. D. A. Kraaijenbrink, A. V. Kulkarni, P. A. Mayewski, S. Nepal, P. Pacheco, T. H. Painter, F. Pellicciotti, H. Rajaram, S. B. Rupper, A. Sinisalo, A. B. Shrestha, D. Viviroli, Y. Wada, C. Xiao, T. dong Yao, and J. E. M. Baillie. Importance and vulnerability of the world’s water towers. *Nature*, 577(7790):364–369, 2020. URL <https://doi.org/10.1038/s41586-019-1822-y>.
- S. Jeffrey, L. Rotstayn, M. Collier, S. Dravitzki, C. Hamalainen, C. Moeseneder, K. Wong, and J. Syktus. Australia’s CMIP5 submission using the CSIRO-Mk3.6 model. *Australian Meteorological and Oceanographic Journal*, 63(1):1–13, 2013. URL <https://doi.org/10.1071/ES13001>.
- J. Jiang, T. Zhou, Y. Qian, C. Li, F. Song, H. Li, X. Chen, W. Zhang, and Z. Chen. Precipitation regime changes in High Mountain Asia driven by cleaner air. *Nature*, 623(7987):544–549, 2023. URL <https://doi.org/10.1038/s41586-023-06619-y>.
- J. H. Jungclaus, N. Fischer, H. Haak, K. Lohmann, J. Marotzke, D. Matei, U. Mikolajewicz, D. Notz, and J. Von Storch. Characteristics of the ocean simulations in the Max Planck Institute Ocean Model (MPIOM) the ocean component of the MPI-

- Earth system model. *Journal of Advances in Modeling Earth Systems*, 5(2):422–446, 2013. URL <https://doi.org/10.1002/jame.20023>.
- V. V. Kharin and F. W. Zwiers. Climate predictions with multimodel ensembles. *Journal of Climate*, 15(7):793–799, 2002. URL [https://doi.org/10.1175/1520-0442\(2002\)015<0793:CPWME>2.0.CO;2](https://doi.org/10.1175/1520-0442(2002)015<0793:CPWME>2.0.CO;2).
- R. Knutti. The end of model democracy? an editorial comment. *Climatic change*, 102(3):395–404, 2010. URL <https://doi.org/10.1007/s10584-010-9800-2>.
- J.-Y. Lee, J. Marotzke, G. Bala, L. Cao, S. Corti, J. P. Dunne, F. Engelbrecht, E. Fischer, J. C. Fyfe, C. Jones, A. Maycock, M. Joseph, O. Ndiaye, P. Swapna, and T. Zhou. Future global climate: scenario-based projections and near-term information. In *Climate change 2021: The physical science basis. Contribution of working group I to the Sixth Assessment Report of the Intergovernmental Panel on Climate Change*, pages 553–672. Cambridge University Press, 2021. URL <https://doi.org/10.1017/9781009157896.006>.
- B. Lehner and G. Grill. Global river hydrography and network routing: baseline data and new approaches to study the world’s large river systems. *Hydrological Processes*, 27(15):2171–2186, 2013. URL <http://doi.org/10.1002/hyp.9740>.
- C. Martinez-Villalobos and J. D. Neelin. Climate models capture key features of extreme precipitation probabilities across regions. *Environmental Research Letters*, 16(2):024017, 2021. URL <https://doi.org/10.1088/1748-9326/abd351>.
- D. Masson and R. Knutti. Climate model genealogy. *Geophysical Research Letters*, 38(8), 2011. URL <https://doi.org/10.1029/2011GL046864>.
- E. C. Massoud, H. K. Lee, A. Terando, and M. Wehner. Bayesian weighting of climate models based on climate sensitivity. *Communications Earth & Environment*, 4(1):365, 2023. URL <https://doi.org/10.1038/s43247-023-01009-8>.
- F. Maussion, D. Scherer, T. Mölg, E. Collier, J. Curio, and R. Finkelburg. Precipitation seasonality and variability over the Tibetan Plateau as resolved by the High Asia Reanalysis. *Journal of Climate*, 27(5):1910–1927, 2014. URL <https://doi.org/10.1175/JCLI-D-13-00282.1>.
- S.-K. Min, D. Simonis, and A. Hense. Probabilistic climate change predictions applying Bayesian model averaging. *Philosophical Transactions of the Royal Society A: Mathematical, Physical and Engineering Sciences*, 365(1857):2103–2116, 2007. doi: <https://doi.org/10.1098/rsta.2007.2070>.
- Y. Nie, H. D. Pritchard, Q. Liu, T. Hennig, W. Wang, X. Wang, S. Liu, S. Nepal, D. Samyn, K. Hewitt, et al. Glacial change and hydrological implications in the

- Himalaya and Karakoram. *Nature reviews earth & environment*, 2(2):91–106, 2021. URL <https://doi.org/10.1038/s43017-020-00124-w>.
- J. Norris, L. M. Carvalho, C. Jones, F. Cannon, B. Bookhagen, E. Palazzi, and A. A. Tahir. The spatiotemporal variability of precipitation over the Himalaya: evaluation of one-year WRF model simulation. *Climate Dynamics*, 49:2179–2204, 2017. URL <https://doi.org/10.1007/s00382-016-3414-y>.
- J. Norris, L. M. Carvalho, C. Jones, and F. Cannon. Deciphering the contrasting climatic trends between the central Himalaya and Karakoram with 36 years of WRF simulations. *Climate Dynamics*, 52:159–180, 2019. URL <https://doi.org/10.1007/s00382-018-4133-3>.
- J. Norris, L. M. Carvalho, C. Jones, and F. Cannon. Warming and drying over the central Himalaya caused by an amplification of local mountain circulation. *NPJ Climate and Atmospheric Science*, 3(1):1, 2020. URL <https://doi.org/10.1038/s41612-019-0105-5>.
- R. Olson, Y. Fan, and J. P. Evans. A simple method for Bayesian model averaging of regional climate model projections: Application to southeast Australian temperatures. *Geophysical Research Letters*, 43(14):7661–7669, 2016. doi: <https://doi.org/10.1002/2016GL069704>.
- A. Orr, C. Listowski, M. Coustet, E. Collier, W. Immerzeel, P. Deb, and D. Bannister. Sensitivity of simulated summer monsoonal precipitation in Langtang Valley, Himalaya, to cloud microphysics schemes in WRF. *Journal of Geophysical Research: Atmospheres*, 122(12):6298–6318, 2017. URL <https://doi.org/10.1002/2016JD025801>.
- A. Orr, B. Ahmad, U. Alam, A. Appadurai, Z. P. Bharucha, H. Biemans, T. Bolch, N. P. Chaulagain, S. Dhaubanjari, A. P. Dimri, H. Dixon, H. J. Fowler, G. Gioli, S. J. Halvorson, A. Hussain, G. Jeelani, S. Kamal, I. S. Khalid, S. Liu, A. Lutz, M. K. Mehra, E. Miles, A. Mombloch, V. Muccione, A. Mukherji, D. Mustafa, O. Najmuddin, M. N. Nasimi, M. Nüsser, V. P. Pandey, S. Parveen, F. Pellicciotti, C. Pollino, E. Potter, M. R. Qazizada, S. Ray, S. Romshoo, S. K. Sarkar, A. Sawas, S. Sen, A. Shah, M. A. A. Shah, J. M. Shea, A. T. Sheikh, A. B. Shrestha, S. Tayal, S. Tigala, Z. T. Virk, P. Wester, and J. L. Wescoat Jr. Knowledge priorities on climate change and water in the Upper Indus Basin: A horizon scanning exercise to identify the top 100 research questions in social and natural sciences. *Earth's Future*, 10(4): e2021EF002619, 2022. URL <https://doi.org/10.1029/2021EF002619>.
- E. Palazzi, J. von Hardenberg, S. Terzago, and A. Provenzale. Precipitation in the karakoram-himalaya: a cmip5 view. *Climate Dynamics*, 45:21–45, 2015. URL <https://doi.org/10.1007/s00382-014-2341-z>.

- T. Palmer, F. Doblas-Reyes, R. Hagedorn, and A. Weisheimer. Probabilistic prediction of climate using multi-model ensembles: from basics to applications. *Philosophical Transactions of the Royal Society B: Biological Sciences*, 360(1463):1991–1998, 2005. URL <https://doi.org/10.1098/rstb.2005.1750>.
- V. M. Panaretos and Y. Zemel. Statistical aspects of Wasserstein distances. *Annual review of statistics and its application*, 6(1):405–431, 2019. URL <https://doi.org/10.1146/annurev-statistics-030718-104938>.
- P. K. Panday, J. Thibeault, and K. E. Frey. Changing temperature and precipitation extremes in the Hindu Kush-Himalayan region: an analysis of CMIP3 and CMIP5 simulations and projections. *International Journal of Climatology*, 35(10):3058–3077, 2015. doi: <https://doi.org/10.1002/joc.4192>. URL <https://rmets.onlinelibrary.wiley.com/doi/abs/10.1002/joc.4192>.
- C. E. Rasmussen and C. K. Williams. *Gaussian processes for machine learning*, volume 1. MIT Press, 2006. URL <https://doi.org/10.7551/mitpress/3206.001.0001>.
- RGI Consortium. Randolph Glacier Inventory—a dataset of global glacier outlines: Version 6.0 [data set]. National Snow and Ice Data Center, 2017. URL <https://doi.org/10.7265/4m1f-gd79>.
- P. Samuelsson, S. Gollvik, M. Kupiainen, E. Kourzeneva, and W. J. van de Berg. The surface processes of the Rossby Centre regional atmospheric climate model (RCA4). Technical report, SMHI, 2015. URL https://www.smhi.se/polopoly_fs/1.89799!/Menu/general/extGroup/attachmentColHold/mainCol1/file/meteorologi_157.pdf. Accessed 18 November 2024.
- B. M. Sanderson and R. Knutti. On the interpretation of constrained climate model ensembles. *Geophysical Research Letters*, 39(16), 2012. URL <https://doi.org/10.1029/2012GL052665>.
- J. Sanjay, R. Krishnan, A. B. Shrestha, R. Rajbhandari, and G.-Y. Ren. Downscaled climate change projections for the Hindu Kush Himalayan region using CORDEX South Asia regional climate models. *Advances in Climate Change Research*, 8(3): 185–198, 2017. URL <https://doi.org/10.1016/j.accre.2017.08.003>.
- A. D. Saul, J. Hensman, A. Vehtari, and N. D. Lawrence. Chained Gaussian processes. In *Proceedings of the 19th International Conference on Artificial Intelligence and Statistics*, pages 1431–1440, Cadiz, Spain, 09–11 May 2016. PMLR. URL <https://doi.org/10.48550/arXiv.1604.05263>.
- E. Snelson, Z. Ghahramani, and C. Rasmussen. Warped Gaussian processes. In *Advances*

- in *Neural Information Processing Systems*, volume 16, Vancouver, BC, Canada, 8–13 December 2003. URL https://papers.nips.cc/paper_files/paper/2003/file/6b5754d737784b51ec5075c0dc437bf0-Paper.pdf. Accessed 11 November 2024.
- D. A. Stainforth, T. E. Downing, R. Washington, A. Lopez, and M. New. Issues in the interpretation of climate model ensembles to inform decisions. *Philosophical Transactions of the Royal Society A: Mathematical, Physical and Engineering Sciences*, 365(1857):2163–2177, 2007. URL <https://doi.org/10.1098/rsta.2007.2073>.
- K. E. Taylor, R. J. Stouffer, and G. A. Meehl. An overview of CMIP5 and the experiment design. *Bulletin of the American meteorological Society*, 93(4):485–498, 2012. URL <https://doi.org/10.1175/BAMS-D-11-00094.1>.
- K. Tazi, A. O. Orr, J. Hernandez-González, S. Hosking, and R. E. Turner. Downscaling precipitation over High-mountain asia using multi-fidelity Gaussian processes: improved estimates from ERA5. *Hydrology and Earth System Sciences*, 28(22):4903–4925, 2024. URL <https://doi.org/10.5194/hess-28-4903-2024>.
- K. Tazi, A. O. Orr, S. Hosking, and R. E. Turner. Precipitation prediction from large-scale climatic features over the Upper Indus Basin using non-stationary Gaussian processes. *Environmental Data Science*, 2025. Accepted.
- C. Tebaldi and R. Knutti. The use of the multi-model ensemble in probabilistic climate projections. *Philosophical transactions of the royal society A: mathematical, physical and engineering sciences*, 365(1857):2053–2075, 2007. URL <https://doi.org/10.1098/rsta.2007.2076>.
- C. Teichmann, B. Eggert, A. Elizalde, A. Haensler, D. Jacob, P. Kumar, C. Moseley, S. Pfeifer, D. Rechid, A. R. Remedio, H. Ries, J. Petersen, S. Preuschmann, T. Raub, F. Saeed, K. Sieck, and T. Weber. How does a regional climate model modify the projected climate change signal of the driving GCM: a study over different CORDEX regions using remo. *Atmosphere*, 4(2):214–236, 2013. URL <https://doi.org/10.3390/atmos4020214>.
- T. Tél, T. Bódai, G. Drótos, T. Haszpra, M. Herein, B. Kaszás, and M. Vincze. The theory of parallel climate realizations: A new framework of ensemble methods in a changing climate: An overview. *Journal of Statistical Physics*, 179:1496–1530, 2020. URL <https://doi.org/10.1007/s10955-019-02445-7>.
- M. Titsias. Variational learning of inducing variables in sparse Gaussian processes. In *Proceedings of the Twelfth International Conference on Artificial Intelligence and Statistics*, volume 5, pages 567–574, Clearwater Beach, FL, USA, 16–18 Apr 2009. PMLR. URL <http://proceedings.mlr.press/v5/titsias09a/titsias09a.pdf>. Accessed 11 November 2024.

- V. Tresp. A Bayesian committee machine. *Neural computation*, 12(11):2719–2741, 2000. URL <https://doi.org/10.1162/089976600300014908>.
- A. Voldoire, E. Sanchez-Gomez, D. Salas y Mélia, B. Decharme, C. Cassou, S. Sénési, S. Valcke, I. Beau, A. Alias, M. Chevallier, M. Déqué, J. Deshayes, H. Douville, E. Fernandez, G. Madec, E. Maisonnave, M.-P. Moine, S. Planton, D. Saint-Martin, S. Szopa, S. Tyteca, R. Alkama, S. Belamari, A. Braun, L. Coquart, and F. Chauvin. The CNRM-CM5.1 global climate model: description and basic evaluation. *Climate dynamics*, 40:2091–2121, 2013. URL <https://doi.org/10.1007/s00382-011-1259-y>.
- M. Watanabe, T. Suzuki, R. O’ishi, Y. Komuro, S. Watanabe, S. Emori, T. Takemura, M. Chikira, T. Ogura, M. Sekiguchi, K. Takata, D. Yamazaki, T. Yokohata, T. Nozawa, H. Hasumi, H. Tatebe, and M. Kimoto. Improved climate simulation by MIROC5: mean states, variability, and climate sensitivity. *Journal of Climate*, 23(23):6312–6335, 2010. URL <https://doi.org/10.1175/2010JCLI3679.1>.
- P. Wester, S. Chaudhary, N. Chettri, A. Maharjan, S. Nepal, and J. Steiner. *Water, ice, society, and ecosystems in the Hindu Kush Himalaya: an outlook*. International Centre for Integrated Mountain Development, Kathmandu, Nepal, 2023. URL <https://doi.org/10.53055/ICIMOD.1028>.
- S. Westermann, C. Barboux, A. Bartsch, R. Delaloye, G. Grosse, B. Heim, G. Hugelius, A. Irrgang, A. Kääb, H. Matthes, I. Nitze, C. Pellet, F. Seifert, T. Strozzi, U. Wegmüller, M. Wieczorek, and A. Wiesmann. ESA Permafrost Climate Change Initiative: Permafrost version 4 data products [data set]. *NERC EDS Centre for Environmental Data Analysis*, 2024. URL <https://doi.org/10.5285/93444bc1c4364a59869e004bf9bfd94a>.
- L. J. Wilcox, Z. Liu, B. H. Samset, E. Hawkins, M. T. Lund, K. Nordling, S. Undorf, M. Bollasina, A. M. Ekman, S. Krishnan, et al. Accelerated increases in global and Asian summer monsoon precipitation from future aerosol reductions. *Atmospheric Chemistry and Physics*, 20(20):11955–11977, 2020. URL <https://doi.org/10.3390/atmos9030080>.
- A. Yatagai, K. Kamiguchi, O. Arakawa, A. Hamada, N. Yasutomi, and A. Kitoh. APHRODITE: Constructing a long-term daily gridded precipitation dataset for Asia based on a dense network of rain gauges. *Bulletin of the American Meteorological Society*, 93(9):1401–1415, 2012. URL <https://doi.org/10.1175/BAMS-D-11-00122.1>.
- M. D. Zelinka, T. A. Myers, D. T. McCoy, S. Po-Chedley, P. M. Caldwell, P. Ceppi, S. A. Klein, and K. E. Taylor. Causes of higher climate sensitivity in CMIP6 models. *Geophysical Research Letters*, 47(1):e2019GL085782, 2020. URL <https://doi.org/10.1029/2019GL085782>.

[//doi.org/10.1029/2019GL085782](https://doi.org/10.1029/2019GL085782).

Appendix A. BCM softmax-variance control

Following Cohen et al. (2020), we use their general expression for expert weights:

$$\beta_j(\mathbf{x}_*) \propto \exp(-1/\psi_j(\mathbf{x}_*)\tau), \quad \sum_{j=1}^M \beta_j(\mathbf{x}_*) = 1, \quad (\text{A.1})$$

where τ is a temperature parameter (with a similar function to T in Section 3.2) that controls the sparsity between experts by multiplicatively compounding the weights of stronger experts. The function $\psi_j(\mathbf{x}_*)$ describes the level of confidence of the j^{th} expert at test point \mathbf{x}_* . Like Cohen et al. (2020), we set $\psi_j(\mathbf{x}_*)$ to the posterior predictive variance at \mathbf{x}_* , i.e., $\sigma_j^2(\mathbf{x}_*)$ and choose $\tau = 1/8$.

Appendix B. Mixture of experts probability distribution

The transformed precipitation \tilde{y} for the r^{th} RCM surrogate at some input coordinate \mathbf{x}_* is assumed to be normally distributed. Suppressing input variables and fixed hyperparameters, we have

$$p_r(\tilde{y}_r) = \frac{1}{\sqrt{2\pi\sigma_r^2}} \exp\left(-\frac{(\tilde{y}_r - \mu_r)^2}{2\sigma_r^2}\right). \quad (\text{B.1})$$

The distribution for y can then be found by transforming the coordinates and calculating the Jacobian $p_r(\tilde{y}_r(y)) \frac{d\tilde{y}_r}{dy}$, yielding

$$p'_r(y) = \frac{y^{\lambda_r-1}}{\sqrt{2\pi\sigma_r^2}} \exp\left(-\frac{\left(\frac{y^{\lambda_r-1}}{\lambda_r} - \mu_r\right)^2}{2\sigma_r^2}\right). \quad (\text{B.2})$$

However, there is a slight issue with this procedure. Inverting the transformation, we find that for $\lambda_r \neq 0$, $y(\tilde{y}) = (\lambda_r \tilde{y} + 1)^{1/\lambda_r}$. This quantity is ambiguous for $\tilde{y}_r < -1/\lambda_r$, as the fractional power of a negative number is ill-defined. To remedy this, we restrict the domain of \tilde{y} to $(-1/\lambda_r, \infty)$, with the cost that we need to renormalise the probability distribution by its integral. Defining

$$C_r := \int_{-1/\lambda_r}^{\infty} d\tilde{y}_r p'_r(\tilde{y}_r) = \int_{-(\lambda_r^{-1} + \mu_r)/\sigma_r}^{\infty} \frac{1}{\sqrt{2\pi}} e^{-x^2/2} = \frac{1}{2} \left(1 + \operatorname{erf}\left[\frac{1}{\sqrt{2\sigma_r^2}} \left(\frac{1}{\lambda_r} + \mu_r\right)\right]\right), \quad (\text{B.3})$$

the properly normalised probability distribution for y is given by

$$p_r(y) = \frac{y^{\lambda_r-1}}{C_r \sqrt{2\pi\sigma_r^2}} \exp\left(-\frac{\left(\frac{y^{\lambda_r-1}}{\lambda_r} - \mu_r\right)^2}{2\sigma_r^2}\right), \quad (\text{B.4})$$

with domain $y \in [0, \infty)$. In practice, we expect C_r to be very close to one.

Finally, given some weights $\{w_r\}_r$, the mixture of experts distribution is given by

$$p(y) = \sum_r w_r p_r(y), \tag{B.5}$$

with the constraint that $\sum_r w_r = 1$.

Appendix C. Which RCMs, when and where?

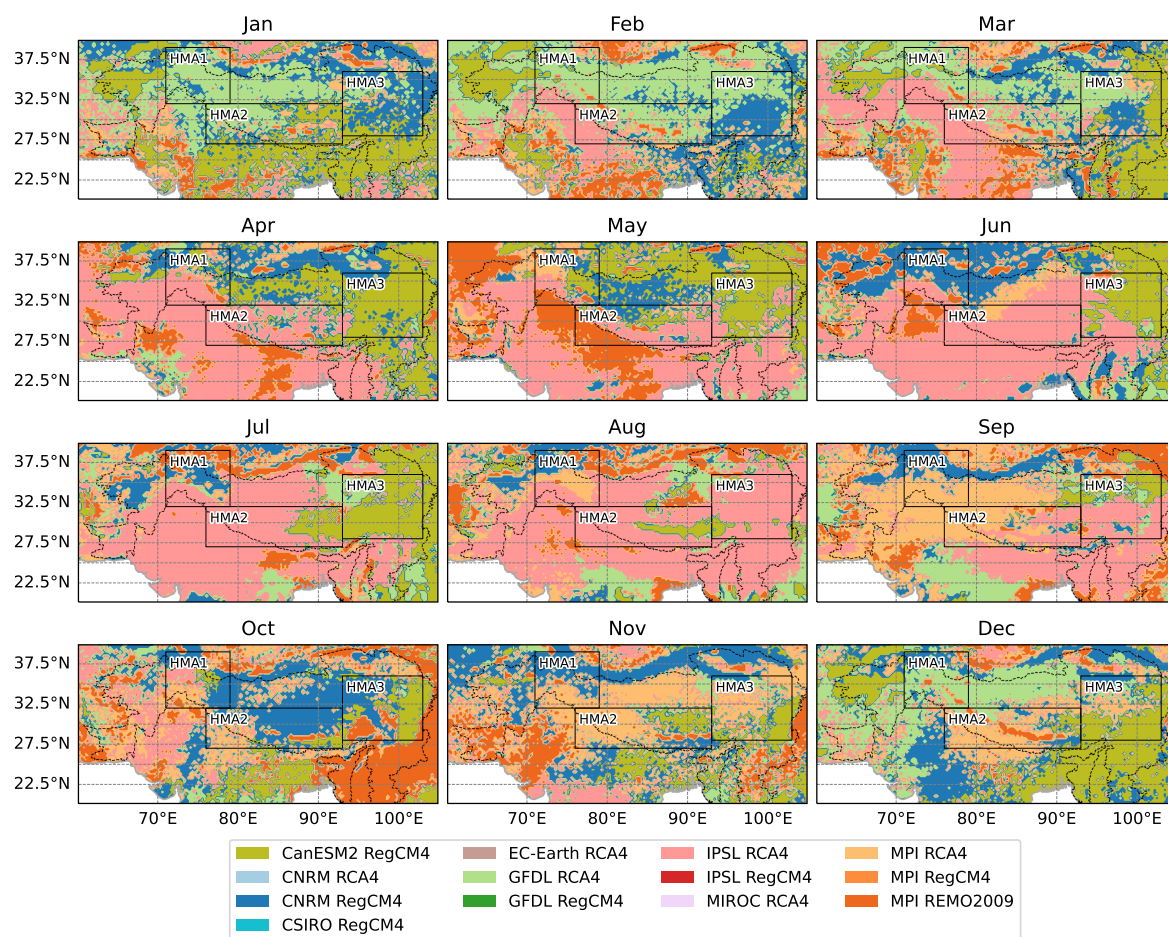


Figure C1. RCMs with the smallest Wasserstein distances for each month and location over HMA. The distances are calculated using the scaled distributions of precipitation between 1951 and 2005. The spatial distribution of these models is not random but follows distinct spatiotemporal patterns.

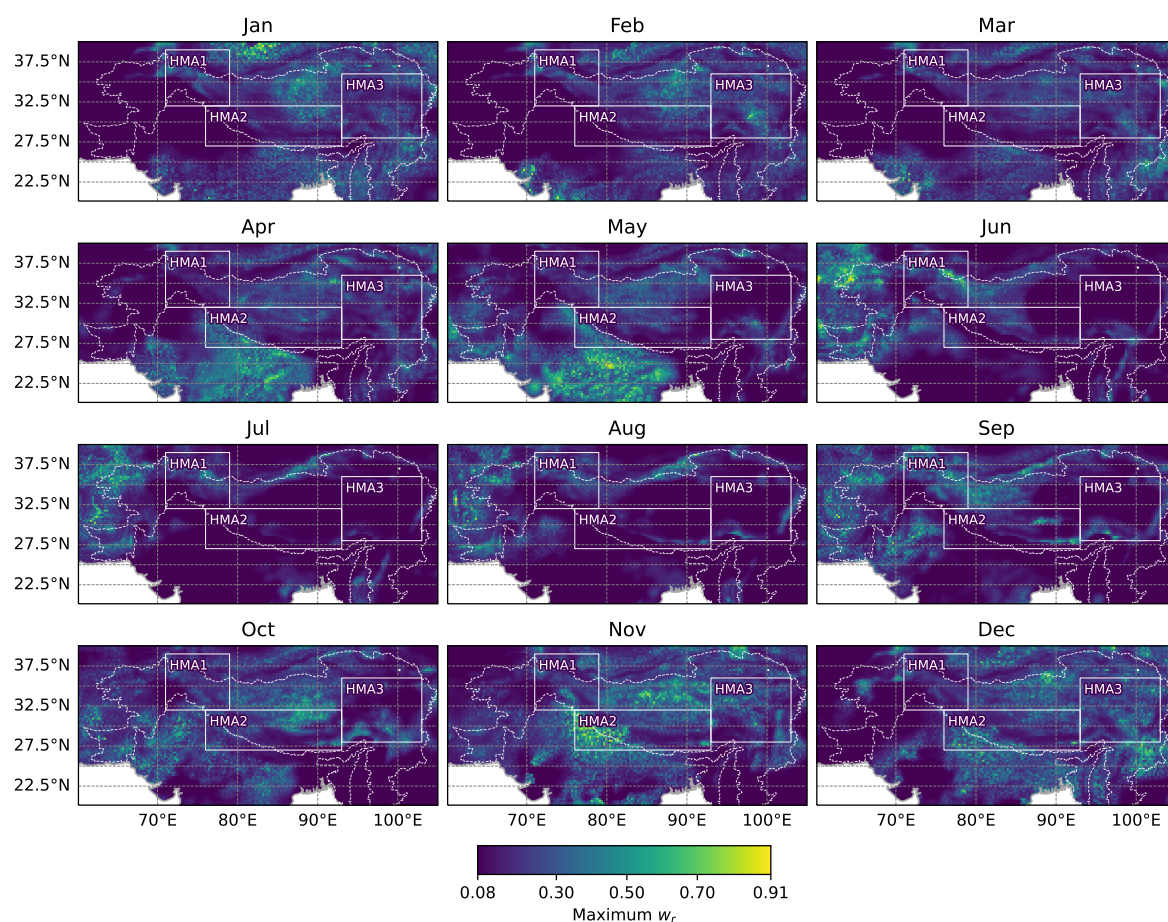


Figure C2. Maximum MoE weights for each month and location over HMA. The weights are optimised between 1951 and 2005. Here, one RCM surrogate (BCM) is never chosen over all others; the maximum w_r is never 1. The maximum BCM weighting is highest over the Hindu Kush during the summer and over the Tibetan Plateau during the winter. Conversely, the MoE with close to equal-weights (i.e. maximum $w_r \rightarrow 1/13$) is more advantageous during the monsoon over the Tibetan Plateau and during the winter over Hindu Kush.

Appendix D. MoE and BCM CRPS differences

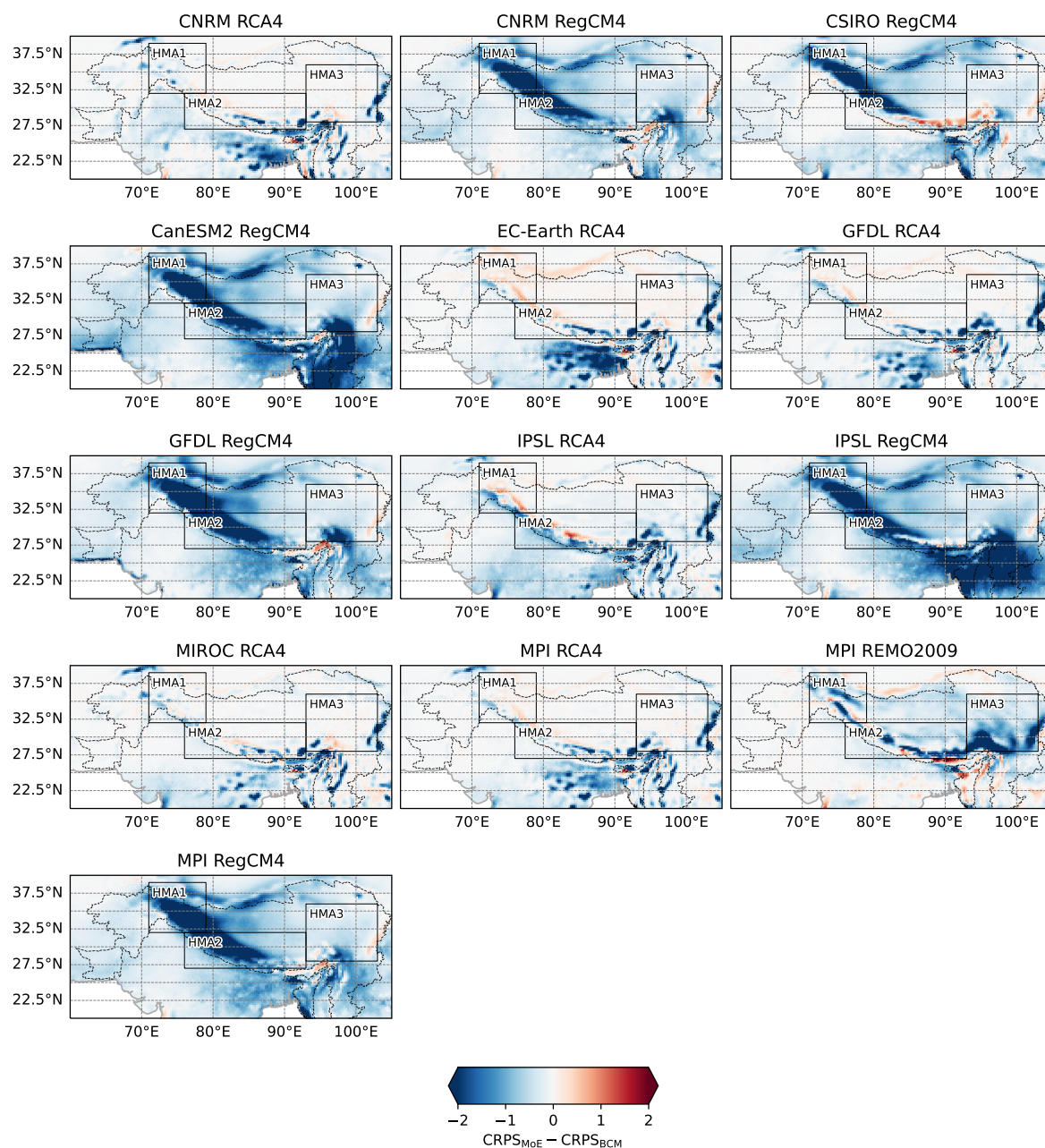


Figure D1. Annual CRPS difference between the MoE and RCM surrogates (BCM) for the held-out validation period (1981–2005). Negative values (blue) imply MoE matches APHRODITE more closely while positive values (red) represent times and location where the BCM performs better. Overall, the MoE outperforms the BCMS over the entire year with large improvement over HM1 and HM2, especially for the RegCM4 surrogates.

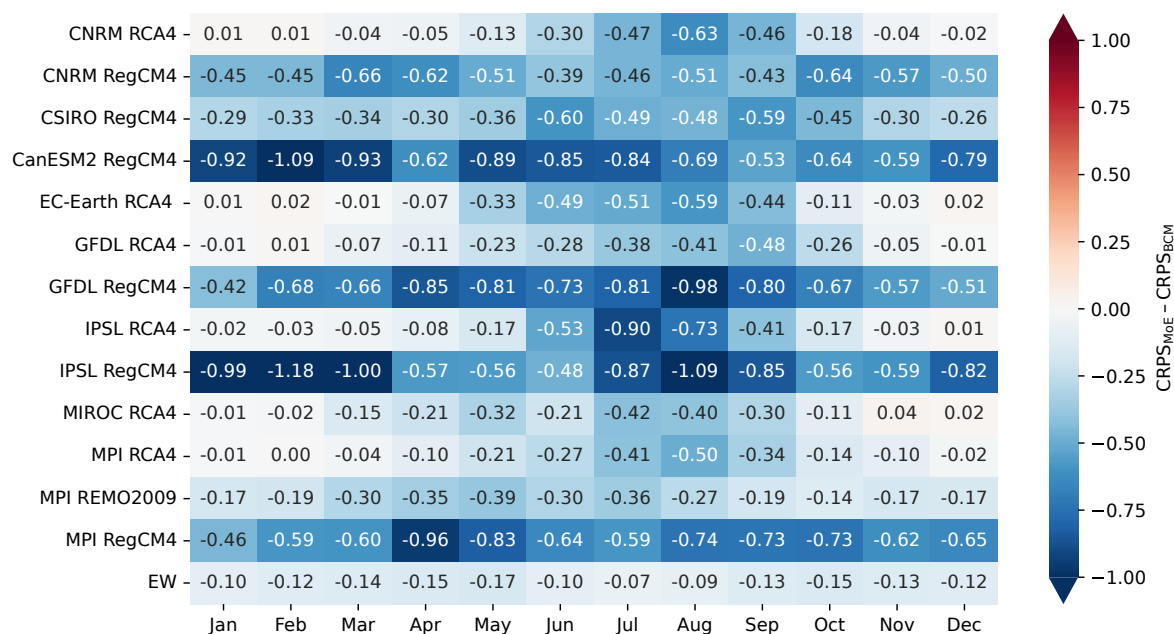


Figure D2. Scorecard showing the differences between the CRPS yielded by the MoE and the CRPS yielded by each RCM surrogate (BCM) as well as the EW over the held out validation period (1981–2005). Each cell represents the difference for a specific model and month, averaged over the entire spatial domain. Positive values (red) indicate higher CRPS for the MoE compared to the BCM, while negative values (blue) indicate lower CRPS for the MoE compared to the BCM.

Appendix E. Near-future predictions

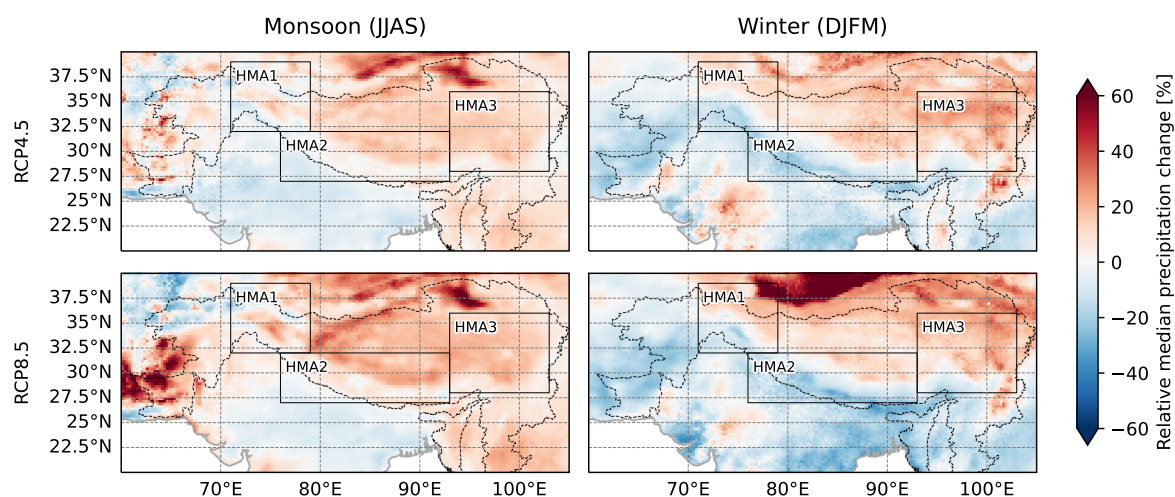


Figure E1. Relative changes between near-future (2036–2065) and historical (1976–2005) MoE precipitation across HMA. The plot shows the median changes for RCP4.5 (top) and RCP8.5 (bottom) during the monsoon (left) and winter (right). Results are similar to far-future predictions with less pronounced changes.

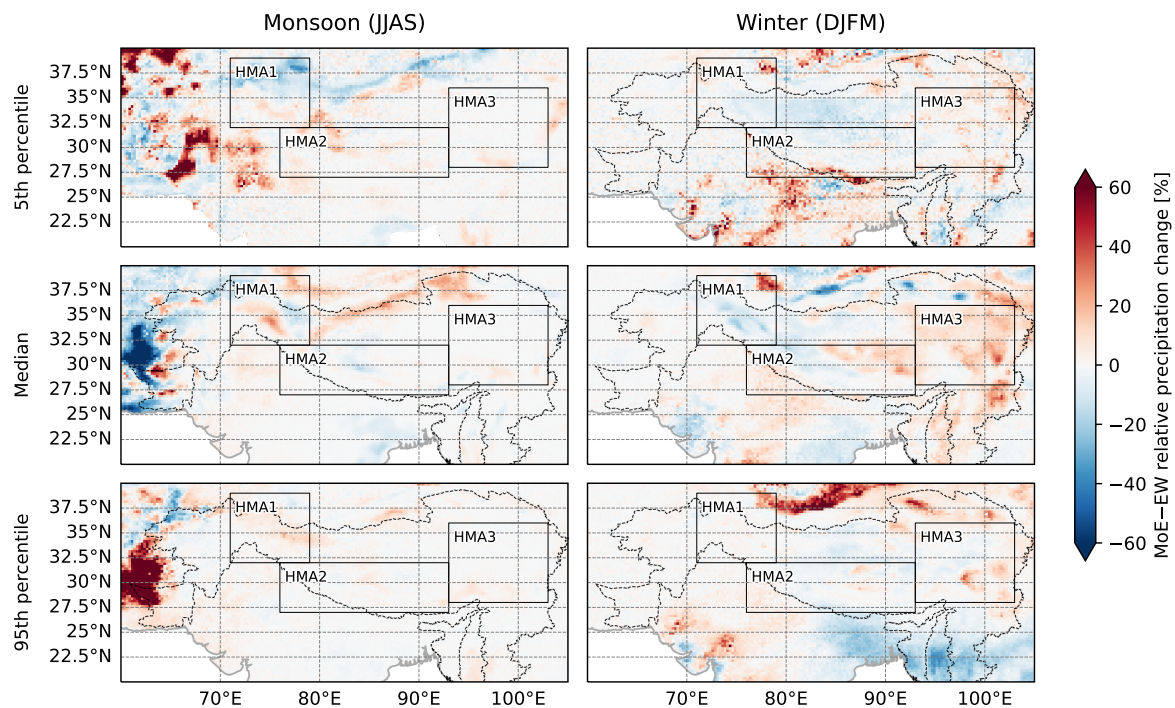


Figure E2. MoE and EW prediction differences for the near future (2066–2095) under RCP8.5 across HMA. The plot shows the difference between the predicted relative changes for the 5th percentile (bottom), median (middle), and 95th (top) during the monsoon (left) and winter (right). Results are similar to far-future predictions with less pronounced differences.